DEVELOPMENT OF A NOVEL CUBESAT DE-ORBITING ALL PRINTED PROPULSION SYTEM

SPACE PROPULSION 2022
ESTORIL, PORTUGAL | 09 – 13 MAY 2022

James Saletes [1], Minkwan Kim [2], Kash Saddul [3], Alexander Wittig [4] , Karim Honda [5], Pekka Katila [6]

[1][2][3][4]*Faculty of Engineering and Physical Sciences, University of Southampton, Southampton, United Kingdom, Email: js10g16@soton.ac.uk, M.K.Kim@soton.ac.uk, Kash.saddul@soton.ac.uk, a.wittig@soton.ac.uk*
[5][6] *Inkron Oy, Espoo, Finland, Email: karim.honda@inkron.com, pekka.katila@inkron.com*

KEYWORDS: Vacuum Arc Thruster, Printed Propulsion System, Printed Electronics, End of Life Deorbiting, Micro propulsion, CubeSat

ABSTRACT:

This study presents the current development status of **Cube**Sat **De**-orbiting **Al**l **P**ropulsion **S**ystem, known as Cube de ALPS through the European Space Agency's Innovative Propulsion System for CubeSats and MicroSats programme. Cube de ALPS is a cluster of vacuum arc thrusters utilising printed electronics and thruster architecture, aiming to expand the orbital potential of ≤ 3U CubeSats. Complying to the IADC post mission disposal time limit of 25 years is challenging for the limited mass, volume and power budgets of CubeSats that prohibit the use of many conventional electrical and chemical propulsion systems. Cube de ALPS focuses on addressing this issue through providing low-cost, fail-safe deorbiting capability.

1. INTRODUCTION

Ever increasing access to space is driving an upsurge CubeSat missions. Many of these missions are run on low budget (on the order of $100,000) on a 6 month to 1-year timescale and led by start-ups or academia. As such, current CubeSat dead-on-arrival rate remains high at 25%. For these missions to access higher Low Earth Orbit altitudes, > 600 km, a form of on-board propulsion would be required to remain compliant with the 25-year Inter-Agency Space Debris Coordination Committee (IADC) end of life de-orbiting time guidelines. This propulsion system would require its own electronic architecture to prevent a dead-on-arrival failure from propagating to the de-orbiting propulsion system.

Cube de ALPS aims to address this problem set through a vacuum arc thruster (VAT) that embraces advances in printing technology to deliver a thin film geometry that can be attached as a standalone system to a ≤ 3U CubeSat. The Cube de ALPS thruster configuration consists of "blocks" of individual thruster "pixels". When an electrical pulse is delivered to the block, a single pixel ignites. This distributes cathode material over multiple pixels removing the requirement for a propellant feed system and arranging these pixels in 3 cm x 3 cm blocks provide attitude control with minimal logic switching between individual pixels. The power processing unit in the Cube de ALPS uses a hybrid inductive, capacitive energy storage to deliver high energy pulses that are required for plasma ignition at about 100 Hz, while maintaining a nominal power of approximately 2 W. This is made possible through a "triggerless" firing mechanism that bridges the gap between the anode and cathode with a thin carbon layer. Parts of this layer are vaporized in the first phase of the pulses to provide a medium for cathode spots to form at a far lower electric field strength than otherwise possible.

The pulsed nature of the VAT enables direct thrust scaling with the input power. This allows compatibility down to the 1U CubeSat level where the power budget available is as low as 2 W. Pulses are delivered to multiple pixels that are distributed across the surface of the system which incorporates redundancy.

Integrating additive manufacturing provides key system advantages. Direct connection between the Power Processing Unit (PPU) and electrodes is made possible to increase electrical efficiency and reduce engineering complexity and harness weight. Production of subsystems can be upscaled with limited capital expenditure, while still enabling thruster geometry to be modified for individual missions based on user requirements.

Figure 1 shows the operational sequence of Cube de ALPS. As can be seen, Cube de ALPS would be in communication with the CubeSat bus. Should the bus be unresponsive, indicating an onboard failure, Cube de ALPS would activate and begin firing with the thrust vector opposing the orbital velocity to accelerate end of life de-orbiting. Should the bus be operational, Cube de ALPS would begin this

sequence once the CubeSat has completed its mission.

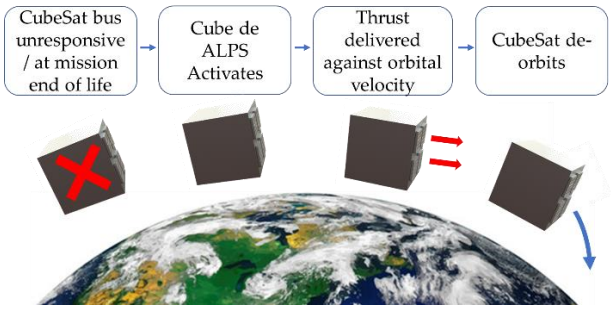

Figure 1: Operational sequence of Cube de ALPS

Though ESA's Technology Development Element programme (TDE), we have developed and manufactured a Breadboard model (BM) of Cube de ALPS. BM Cube de ALPS has been tested at the European Space Research and Technology Centre (ESTEC) through a two-week test campaign to assess plume distribution and system endurance. In this study, we present the details of key findings on Cube de ALPS development programme.

1.1 Vacuum Arc Structure and Ion Acceleration

Cube de ALPS generates thrust upon the principle of vacuum arcs, also known as cathode spots, which eject high velocity plasma of ion velocities up to 30,000 ms^{-1}[1]. Vacuum arcs are widely used in industry to control the solidification of segregation sensitive metal alloys and to produce intense beams of positive ions such as ion implantation, thin film deposition of hard coatings, and transparent conducting oxides. The physical process of vacuum arc formation, therefore, has been well documented in past publications [2], [3].

A vacuum arc is a high-current density, low-voltage (between 16 V and 32 V) electrical discharge that produces a plasma consisting of vaporized and ionised electrode material. In the vacuum arc, the main plasma source is cathode spots. Cathode spots are small, between 1 μm and 100 μm depending on the discharge, and fast moving along the cathode surface, between 100 and 300 m/s. Joule heating caused by the high current densities of the cathode spot vaporise cathode material, eroding small craters into the cathode material. As these craters grow over the spot lifetime, Joule heating is reduced thus the cathode spot can no longer be sustained. A new cathode spot can be formed at high points on the cathode near the previous spot location when an electric field is maintained between electrodes [4].

Figure 2 shows a schematic of the cathode spot structure. As can be seen, it consists of ballistic, heavy particle relaxation, electron beam relaxation and expansion area zones. When a cathode spot occurs, ~ 100 μm radius area on the cathode is heated and its material is evaporated. The vaporised cathode material is ionised along four general zones. The vaporised cathode material is separated from the cathode surface by a very thin zone which is about 1 ~ 10 nm. This thin layer zone is a collisionless sheath, also called a ballistic zone. In the ballistic zone, both ions and electrons are experiencing a high electric field which is created by the space charge of ions and can be modelled by collisionless equations. The ballistic zone also hosts a backflow of electrons and ions from upper regions of the spot that act as a key contributor to the Joule heating phenomena. After the ballistic zone, it has a relaxation zone for heavy particles, which extends about 10 nm from the cathode. Here, the emitted neutral atoms collide with each other and the backflow of heavy particles resulting in the Maxwellian distribution. The emitted electrons carry the most of arc current and form a beam. This area is known as an electron beam relaxation zone. In the electron relaxation zone, an electron beam is accelerated toward an anode by the electric potential seen in the ballistic zone. This is randomised by collision with heavy particles up to about 1 μm from the surface. Beyond this zone, a dense plasma expands into vacuum, which can be used to generate a thrust [5].

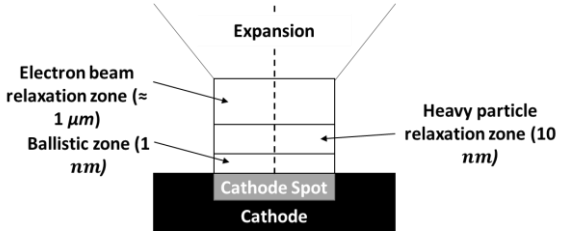

Figure 2: A Schematic of cathode spot structures.

Figure 3 shows the ionisation process in a vacuum arc. As can be seen, the emitted electrons and atoms from the cathode spot collide in the pre-sheath region resulting in a cloud of positively charged ions and electrons characterised as the arc plasma. Some of the electrons and ions return to the surface of the cathode. These returning ions are important to allow for reignition of the vacuum arc. Between 7 and 12% of the electrical discharge current is converted to the ion current flux [1]. The total ionisation rate is typically greater than 99% which can be demonstrated by the production of multiple charged ions seen in most metals [6].

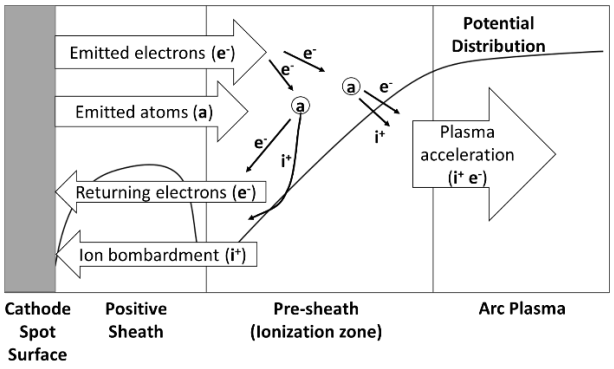

Figure 3: Illustration of a vacuum arc in the vicinity of a cathode spot with overlayed potential distribution where 'a' is a cathode atom, i+ is an ion and e- is an electron.

The plasma emitted from the cathode spots has a high density that can reach values of up to $10^{26}\,m^{-3}$ in the proximity of the cathode spot and about $10^{20}\,m^{-3}$ at few millimetres from the cathode spot. The emitted plasma is accelerated to high velocities within a few hundreds of micrometres of the cathode spot by electron pressure gradient and electrostatic forces created by a potential hump. Ion velocity of plasma is in the order of magnitude of $10^{4}\,m/s$, with variation between different cathode materials. As the plasmas produced in cathode spots are highly directional, they can be used to produce thrust directly.

1.2 VAT Operation for CubeSats

A minimum field strength on the order of 15 to 30 x $10^{6}\,V/m$ is required to trigger the electron discharge from the cathode to the anode in free space to then trigger the vacuum arc process. This is challenging to accomplish on a system designed around CubeSat power constraints. André Anders *et al* has overcome this issue using a "triggerless" firing mechanism [7]. The triggerless firing mechanism applies a thin conductive layer between the anode and cathode across the insulator with a high but finite resistance of approximately 1 $k\Omega$. Applying a sufficiently high voltage, on the order of a few hundred volts, results in breakdown in small gaps within this conductive layer. The produced vapor enables the ignition of the main discharge gap. For reliable and continued operation, the insulator should be selected to withstand the high localised temperatures of the vacuum arc. Alumina ceramic is typically used.

Sustaining plasma formation requires relatively low voltages of between 15 and 32 V, dependent on the cathode material, and a power supply sufficient to sustain the current of a few Amperes. The power constraints of CubeSats make it impossible to operate a vacuum arc thruster in a continuous mode. Pulsed operation, therefore, should be used. This allows for a highly scalable system where the pulsing frequency can be amended depending on the power available. In the pulsed operation, the amplitude and duration of the current pulse can affect the thrust efficiency. We, therefore, need to optimise the duration and amplitude of the current pulse.

2002 saw a new type of inductively driven PPU that shrunk the power electronics of a VAT system at CubeSat level [8]. A short, 1 μs, peak voltage of a few hundred volts is generated by rapidly switching off the current through an inductor. This partially vaporises the conductive layer to provide a medium through which a vacuum arc can form, dropping the resistance of the system and allowing the remaining energy stored in the inductor to do discharge through this vacuum arc at the plasma voltage. Storing all the energy in the inductor in this way is however problematic from a mass perspective. The thick iron core of the inductor resulted in it occupying 90% of the mass of the PPU. Therefore, this principle has since been adapted to incorporate a capacitor to the charging cycle and sustain the plasma voltage after ignition. This both bolsters efficiency and reduce the size of the inductor required.

Figure 4 shows a schematic of the capacitive-inductive PPU. The plasma voltage of between 15 and 32 V, depending on the cathode material, is supplied to the PPU. When a square-wave input signal is applied to the insulated-gate bipolar transistor (IGBT) on the PPU, it will complete a circuit thus building up an electromagnetic charge in the inductor as the capacitor discharges to ground. This is called the 'inductor charging period'. The charging period is determined by the inductance (L) and capacitance (C) of the PPU. The duration of the charging period can be controlled by the length of the pulse-width modulated input signal on the IGBT and set to the point of peak charging current. After the charging period, circuit loop 1 can be opened by turning off input signal. Then, the energy stored in the inductor will be released in a high voltage pulse which is defined by $L\frac{dI}{dt}$. The produced high voltage pulse will cause breakdown between the anode and cathode through a conductive layer thus closing circuit loop 2. This process will lead to the production of cathode arc plasma which expands from the cathode and thereby produces thrust. The relatively low voltage of the arc can be sustained for sum microseconds by the energy stored in the capacitor as it discharges. The energy stored in the inductor should equal the energy stored in the capacitor at point of discharge in order to optimise PPU efficiency [9].

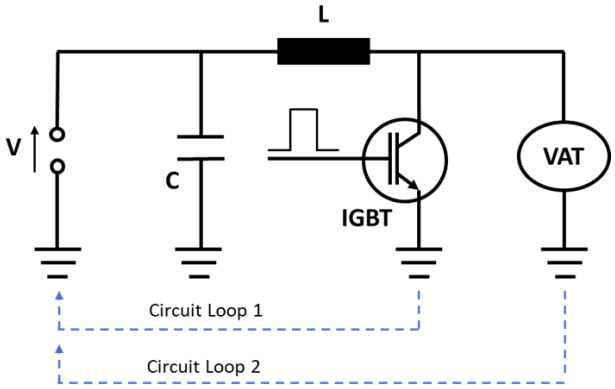

Figure 4: Simplified schematic of the inductive-capacitive power processing unit to drive a VAT.

2. PRINTED ELECTRONICS

Printed electronics offer a new way to manufacture electronics utilising old manufacturing methods such as screen printing, combined with novel materials, which provide design opportunities. The printed electronics technology is universal as the applications are broad and diverse as this same manufacturing technique can be applied to the coaxial electrodes with the thruster heads of the VAT. This eliminates the need for an interface between the electronics and thruster, reducing system complexity and manufacturing time. The impact of flexible, printed electronics ranges from straightforward mass, volume, and cost savings all the way to enabling new mission concepts. Several key advantages that can be taken advantage of have been illustrated below.

Flexibility: The flexible substrate of a printed propulsion system provides many options for storage and deployment. Reconfiguring on orbit or after deployment enables a third dimension to be realized for additional structural rigidity, improved performance (antenna or optics shape), or even mobility. Conformability to surfaces is advantageous in many engineering applications to improve sensing or to fit with existing hardware/infrastructure designs.

Low recurring costs: Depending on the specific system and manufacturing approach, the cost of recurring engineering may be less than a traditional assembled propulsion system. This makes it an attractive platform for large numbers (mega-constellations) or “disposable” systems through mass production.

Low mass & volume: The mass and volume of the system is significantly reduced from a conventional subsystem using PCB (printed circuit board) because subsystems are applied to light-weight thin substrates. The thin sheets of printed systems make a printed propulsion system attractive as a “propulsion sticker”. Accommodating and stowing large numbers of systems is simpler when systems can be attached to the external surface of a spacecraft.

Short cycle time: For a printed propulsion system, the design paradigm shifts away from mechanical packaging challenges to a focus on electrical layouts and fabrication flow. Control/communication systems and power processing units can be printed easily by a number of lab-scale printers allowing system designs to be prototyped, tested, and modified quickly. Manufacturing of the system will span days, not months due to the reduction of touch labour. Testing can be done in parallel on multiple copies, rather than serially on a qualification and flight unit. All these effects result in shorter development times which in turn help contain costs.

Robustness: The nature of the construction provides the propulsion system a certain robustness over traditional subsystem manufacturing. By implementing mechanically robust “ink stacks”, the printed propulsion system is more resilient to structural loading environments such as launch, landing, and shock, which will ensure fail-safe operation of the printed propulsion system as a de-orbiting mechanism.

The printed electronics manufactured for this study include inductors, resistors, and capacitors. These passive components were screen printed by Inkron using their silver ink IPC-605X (Inkron Oy) as the primary conductor and their carbon ink IPC-631 (Inkron Oy) where required.

2.1 Printed Inductor

The concept for a printed inductor is to print a spiral pattern of conductive ink onto a substrate. An example of this concept is shown in Figure 5 with its inductance calculated from the square form of the modified Wheeler formula presented as:

$$L = K_1 \mu_0 \left(\frac{n^2 d_{avg}}{1 + K_2 \rho} \right) \qquad \text{Eq. 1}$$

where L is the inductance in Henrys, K_1 and $K_1$are coefficients for the square geometry of 2.34 and 2.75 respectively, μ_0 is vacuum permeability of 1.26 x 10^{-6} F/m, n is the number of coils, d_{avg} is equal to half the sum of the inner and outer diameter of the coil and ρ is the filling ratio defined as [10]:

$$\rho = \frac{d_{out} - d_{in}}{d_{out} + d_{in}} \qquad \text{Eq. 2}$$

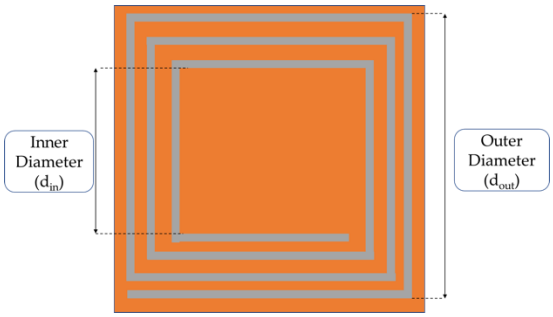

Figure 5: Schematic of a square printed inductor.

The targeted value of inductance for the Breadboard Model of the Cube de ALPS PPU (BMPPU) was 120 μH. To assess the feasibility of this, test coils were manufactured of scaling diameter from 7.5 mm to 17.5 mm in 2.5 mm increments. Test coils were also manufactured scaling the conductive track width and separation between 150 μm and 350 μm in 50 μm increments.

2.2 Printed Resistor

The concept of a printed resistor is to print two silver conductive tracks connected by a resistive carbon layer. Through this method the resistance can be tailored to the desired value by varying the width of this track, w, the track separation distance, l, and depth of the carbon ink track. A schematic of this layout is shown in Figure 6.

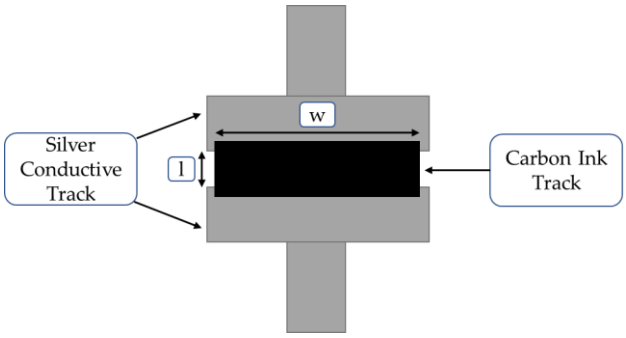

Figure 6: Schematic of a printed resistor.

The BMPPU requires 1 $k\Omega$ of resistance. Sample resistors have been printed to a range of 200 Ω to 20 $k\Omega$ on both a Kapton film and directly onto the Printed Circuit Board (PCB).

2.3 Printed Capacitor

Fig. 7 shows a schematic of a printed capacitor. The concept of a printed capacitor circuit is to print a thin layer of conductive material onto a thin substrate and then to repeat the process on the other side. One side is connected to a positive terminal and the other side is connected to ground. This produces a capacitor whose capacitance can be predicted through:

$$C = \frac{\varepsilon_r \varepsilon_0 A}{d} \qquad \text{Eq. 3}$$

where C is capacitance, ε_r is relative permeability of the dielectric material (4.2 for Kapton and between 3 and 4 for Polyethylene Terephthalate (PET) [11]) and ε_0 is vacuum permittivity of free space (8.857 x 10^{12} F/m), A is the effective capacitive area of the two parallel plates and d is the separation distance between the two plates or equivalently the thickness of the dielectric layer.

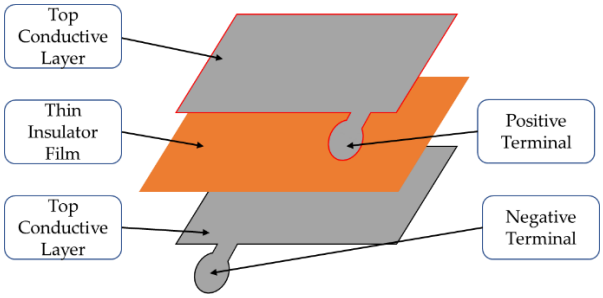

Figure 7: Schematic of a printed capacitor.

The targeted capacitor value for the BMPPU is 0.2 uF. Cube de ALPS is targeted for the 1U CubeSat class and so the available area is limited to 10 cm x 10 cm and the sample size of each capacitor layer shall fit within this range. Two insulators were used in the manufactured samples, 7.5 μm Kapton and 1.4 μm PET. The overlapping conductive area used for these samples was 7 cm x 8 cm due to the availability of Kapton at 7.5 μm.

2.4 Printed Electronics Results

Table 1 presents the measured results of the largest printed inductor sample manufactured, with a diameter of 17.5 mm and an inductance of 1.9 μH. Larger samples were not produced due to the high measured resistance of 200 Ω. This resistance is prohibitive for the use in the BMPPU and scaling the inductor up to achieve the desired 120 μH would only increase this further. The design used for the inductor test samples could be used in other PCB applications where a resistor with resistance below 200 Ω would be required. This is because the printing of a resistor to a resistance below this level is challenging when using the printed resistor method described in section 2.2 as it requires a high print precision to print the conductive tracks close enough without touching. Figure 8a shows the printed inductor sample.

Table 1: Measured parameters of the largest printed inductor sample produced.

Inductor Parameter	Value	Units
Desired inductance for BMPPU	120	μH
Achieved inductance	1.9	μH
Inductance variation	n/a	%
Substrate	Kapton	n/a

Substrate thickness	0.05	mm
Cured ink thickness	0.018	mm
Mass (includes ink and substrate with an additional 1 mm perimeter)	0.47	g
Inductor sample area	3.1	cm^2
Volume (printed area times total thickness)	21 x 10^{-3}	cm^3

Table 2 lists the measured results of the printed resistor when printed directly onto the PCB and when printed onto a thin, flexible substrate. When printing to a flexible substrate the resistance values were constantly within a ±20% range. Printing directly onto the PCB proved more challenging as the PCB coating appeared to interfere with the resistor during the curing process. However, after several attempts, two resistors were printed onto BMPPU within the ±20% range. This tolerance can be improved by larger prints or through a more accurate printing method. Figure 8b shows the printed resistor printed directly to the PCB and Figure 8c shows a manufactured printed resistor on a thin, flexible substrate.

Table 2: Measured parameters for the printed resistor. The rows for desired resistance, achieved resistance and resistance variation are the measured values when printed onto BMPPU. The remaining rows are measured values when printed to a thin film substrate.

Resistor Parameter	**Value**	**Units**
Desired resistance	1	$k\Omega$
Achieved resistance	1.1	$k\Omega$
Resistance variation across samples	±20	%
Substrate	PET	n/a
Substrate thickness	0.15	mm
Cured ink thickness	0.025	mm
Mass (includes ink and substrate with an additional 1 mm perimeter)	0.011	g
Resistor sample area	0.25	cm^2
Volume (printed area times total thickness)	4.3 x 10^{-3}	cm^3

Table 3 presents the measured results of the printed capacitor. Two dielectric substrates were used, 7.5 μm Kapton and 1.4 μm PET. When using Kapton, the measured capacitance for a 7 cm x 8 cm was 0.025 μF ±20%. When using PET, many of the prints were not successful as the very thin substrate would tare during the printing process and would cause a short circuit. When printing was successful the capacitance was 0.075 μF ±20%. Three layers of the PET capacitors were stacked and connected in parallel to produce the capacitor described in Table 3. Each layer was placed on a 0.15 mm thick PET substrate for structural support. The printed capacitor that was attached to the BMPPU is shown in Figure 8d.

Table 3: Measured parameters for the printed capacitor applied to BMPPU.

Capacitor Parameter	**Value**	**Units**
Desired capacitance	0.2	μF
Achieved capacitance	0.22	μF
Capacitance variation across samples	±20	%
Dielectric substrate	PET	n/a
Dielectric substrate thickness (per layer)	1.4	μm
Supporting substrate	PET	n/a
Supporting substrate thickness	0.12	mm
Total substrate thickness (three dielectric substrates and three supporting substrates)	0.45	mm
Total cured ink thickness (across three layers)	0.16	mm
Total Mass, includes dielectric substrate x 3, supporting substrate x 3 with an additional 10 mm perimeter)	11.5	g
Capacitor area	56	cm^2
Total Volume (printed area times total thickness)	1.2	cm^3

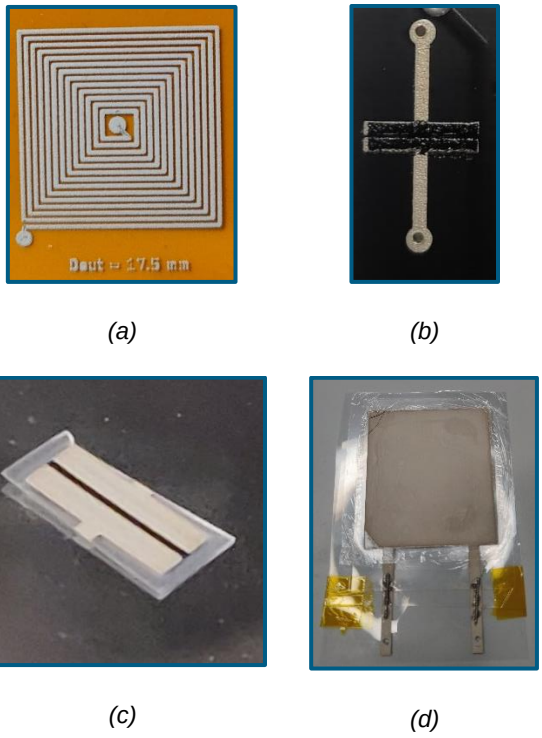

(a) *(b)*

(c) *(d)*

Figure 8: Manufactured printed electronic components. a) Printed inductor sample. b) Printed resistor printed onto BMPPU. c) Printed resistor printed on a thin film substrate. d) Printed capacitor that was connected to BMPPU.

3. CUBE DE ALPS BREADBOARD MODEL ARCHITECTURE

The breadboard model of Cube de ALPS is divided into the three subsystems, BMPPU, Breadboard Model Controller (BMC) and Breadboard Model Vacuum Arc Thruster (BMVAT). A printed (P-BMVAT) and machined (M-BMVAT) BMVAT are manufactured and tested.

3.1 Power Processing Unit (BMPPU)

The BMPPU uses a capacitive-inductive energy storage system to deliver the ignition voltage for triggerless operation and to sustain the plasma voltage after ignition. 27 V was delivered to the BMPPU, the primary capacitor has a capacitance of 330 μH and the inductor has an inductance of 120 μH.

The BMPPU operates in three phases. In phase one, the input power is opened to the capacitor allowing it to charge. In phase two, the input power is disconnected, and the capacitor is shorted to ground through the inductor. The current peaks at 40 A. In phase three, the power supply remains disconnected, and the capacitor is disconnected from ground. This causes a rapid rate of change of current through the inductor resulting in a short voltage peak of up to 1.1 kV for 1 μs. This is supplied across the anode and cathode of the BMVAT where breakdown occurs. The remaining energy stored in the inductor and capacitor discharge through the cathode arc until it can no longer be sustained. This is typically 40 μs but can vary depending on the initial energy required for breakdown.

Two resistors of 1.1 $k\Omega$ were printed onto the surface of the BMPPU and a printed capacitor of 0.22 μF was connected. The PPU board is 5 cm x 10 cm and attached to a larger, 10 cm x 10 cm interface board that allows for easy interfacing with diagnostics and other subsystems. The BMPPU is shown in Figure 9.

Figure 9: BMPPU.

3.2 Controller (BMC)

The BMC provides a 5V, two channel digital signal. The first channel controls an IGBT that opens and closes the circuit between the power supply and the BMPPU. The second controls an IGBT that opens and closes the circuit between the primary capacitor and ground. The second channel also provides the signal through which an oscilloscope is triggered to acquire voltage and current data. The frequency and duration of these pulses are controlled through an Arduino controller and be calibrated depending on the power supply internal resistance.

3.3 Vacuum Arc Thrusters (BMVAT)

Two models of the BMVAT were produced and tested, a printed version and a machined version. Each version comprised blocks of 25 pixels arranged in a 5 x 5 grid. Within each pixel, the cathode diameter is 1.7 mm, the gap between the anode and cathode is 0.4 mm, the anode exit aperture is 4.5 mm, the depth of the anode is 1.4 mm for the P-BMVAT and 1 mm for the M-BMVAT. This difference is because of the SLS printing limitation of printing sharp corners. The depth of the cathode is 2.5 mm. The thin conductive layer was NovaCentrix jr-700lv carbon ink. This configuration is shown in the cross section of a pixel in Figure 10.

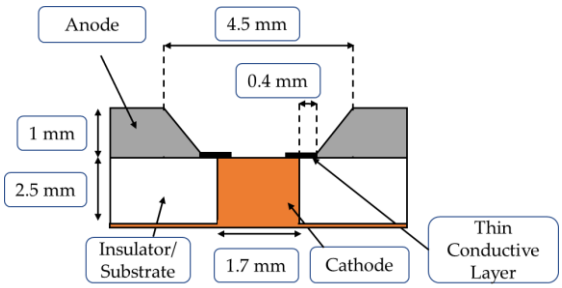

Figure 10: Schematic of a cross section of a single pixel in the BMVAT.

In the P-BMVAT, the cathode material is Inkron's silver ink, IPC-605X. This ink comprises of silver micro particles (87% wt) embedded within a siloxane polymer matrix (13% wt) and was injected into predrilled holes into the Macor substrate. A single print layer electrically connected all of the cathodes within the block. The anode was printed using selective laser sintering (SLS) out of stainless steel.

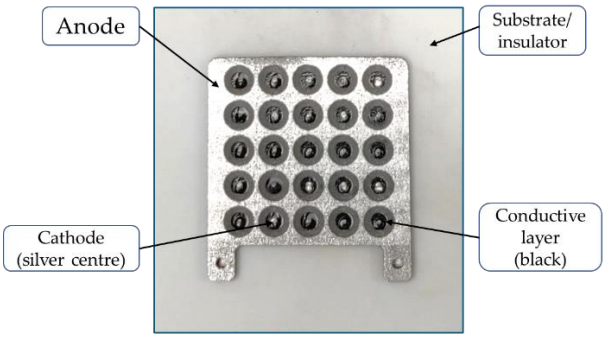

Figure 11: P-BMVAT

The M-BMVAT comprised two blocks of Computer Numerical Control (CNC) machined components, one using an aluminium cathode and one using a copper cathode. The anode was stainless steel, and the insulator was alumina bushes, one per pixel.

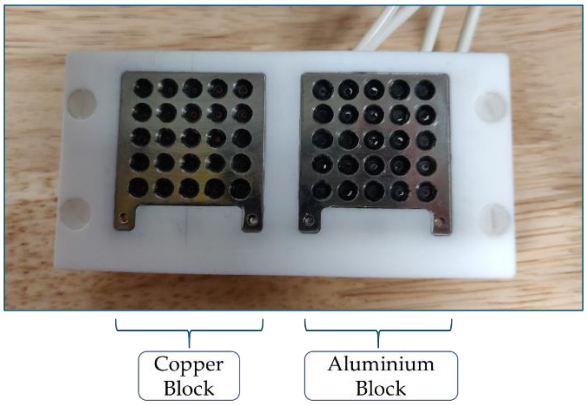

Figure 12: The M-BMVAT. Copper cathode block on the left-hand side. Aluminium cathode block on the right-hand side.

4. EXPERIMENTAL DESIGN

The breadboard model of Cube de ALPS was taken to ESTEC in the ESA Propulsion Lab (EPL) for a two-week test campaign. Tests were performed in the FEEP VF facility at pressures below $10^{-5} mb$. Plume distribution and endurance tests were carried out on the P-BMVAT and the M-BMVAT using both the aluminium and copper cathode blocks.

4.1 Plume Distribution Setup

When an electrical pulse is delivered from the BMPPU to the BMVAT, a single pixel with the lowest impedance ignites. Once the thin conductive layer has been applied to all of the pixels, it is not possible to determine which pixel will ignite and this pixel changes between ignitions. Should the same pixel ignite, the cathode arc may form on a different part of the pixel. Therefore, to characterise the plume distribution of a single pulse, the ion current should be collected simultaneously at different angles relative to the normal of the thruster.

For this purpose, a two-axis diagnostic arm was manufactured at ESA. Each axis was equipped with 5 Faraday Cups (FC) at angles -73°, -32°, 0°, 32° and 72° for a total of 9 (the 0 ° FC is the same for both axes). The FCs were mounted 19 cm from the mounted BMVAT with the stainless-steel shield negatively biased to -60 V and the collector negatively biased to -118 V. Figure 13 shows the data acquisition arm with the P-BMVAT mounted in position.

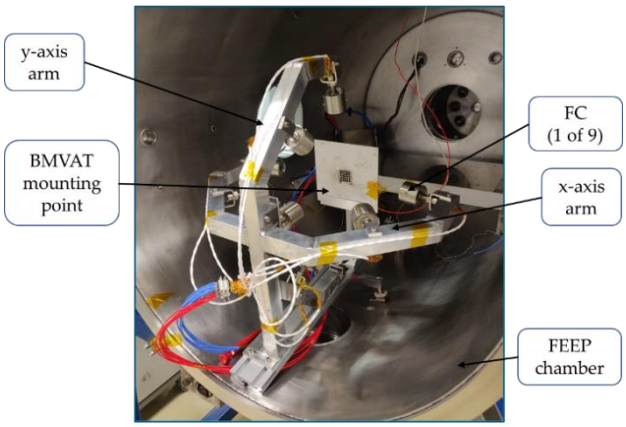

Figure 13: Plume diagnostic arm in the FEEP chamber with the PBMVAT mounted.

The FC data acquisition rate was 10 kHz. Higher aquation rates were attempted but proved unstable. The typical pulse duration was 40 μs with the ion current decaying exponentially over that time. Consequently, the data collected was not able to provide an empirical estimate of the magnitude of the total ion current. However, the data collected can and has been used to compare the relative magnitudes of the peak ion currents to determine the distribution of the plume.

4.2 Endurance Setup

The plume diagnostic arm was removed for the endurance test to prevent any spluttering damaging the FCs. The P-BMVAT and M-BMVAT were mounted in the FEEP chamber and pulses delivered at a frequency of 100 Hz. The endurance was considered complete once the duration of the discharge current fell below 1 μs averaged over 512 pulses.

Figure 14 shows the endurance setup in the FEEP chamber and taken over a two second exposure during the endurance test of the P-BMVAT. Multiple pixels can be seen to be ignited.

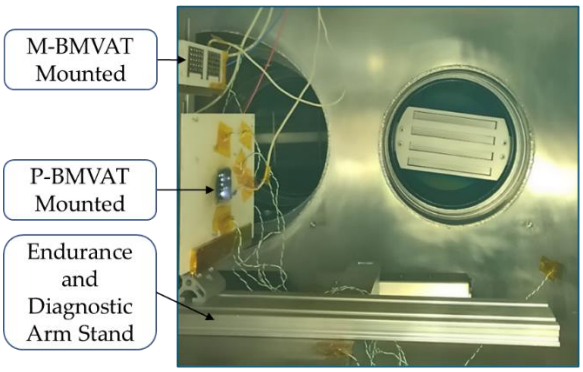

Figure 14: The M-BMVAT and the P-BMVAT mounted for the endurance test. Image taken over a 2 second exposure while P-BMVAT is firing.

5. RESULTS

Figure 15 shows a typical discharge pulse profile delivered by the BMPPU to the BMVATs during operation. The pulse duration is 50 μs with a peak discharge current of 10.25 A. This current rapidly decays as energy is depleted from the inductor and capacitor in the PPU. The voltage rises sharply over the course of 1 μs until a cathode arc forms over one of the pixels. In the case presented in Figure 15, this breakdown voltage was 450 V. The cathode arc provides a low resistive path for the remaining energy in the PPU, allowing the voltage to drop to the plasma voltage of 24 V for the duration of the discharge. This pulse was delivered for the plume distribution tests and the start of the endurance tests. The magnitude and duration of the discharge current decreased over the endurance test as more of the PPUs energy was required for ignition.

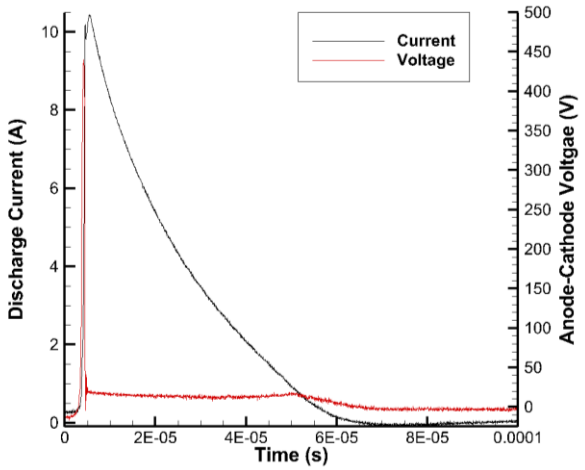

Figure 15: Discharge pulse profile. The recorded voltage between the anode and cathode is shown in red and the discharge current is shown in black.

5.1 Plume Distribution Results

Data from 1000 pulses from the P-BPPU, 4000 pulses from the M-BMVAT with the aluminium cathode and 5000 pulses from the M-BMVAT with the copper cathode was collected. Each of these pulses provided nine data points, one for each of the acquiring FCs. These nine data points were then grouped and averaged into three categories, one representing the 0° FC, the second representing the four FCs placed at 32° from the thruster axis and the third representing the four FCs placed at 74° from the thruster axis. These three points were then normalised to one to account for variations in their relative magnitude. The standard deviation of each of these values was about 0.015 and is plotted for each point in Figure 16 - Figure 18.

A cosine distribution with the general equation:

$$y = a\cos(bx) \qquad \text{Eq. 4}$$

where y is the normalised current density for a given value of x which is the plume angle in degrees. a and b are constants fitted to best represent the recorded data using the Curvefit tool in Matlab. Table 4 presents the values of these constants as well as well as the proportion of the variation in the measured data to that predicted by the cosine distribution through the R^2 value. Figure 16 - Figure 18 present the normalised plume distribution data and the fitted cosine distribution for the three VATs tested.

Table 4: Fitted cosine distribution constants and R^2 for the three VATs tested.

VAT	a	b	R^2
P-BMVAT	0.5263	1.19	0.9516
M-BMVAT with aluminium cathode	0.4948	1.0789	0.9953
M-BMVAT with copper cathode	0.4920	1.0835	0.9832

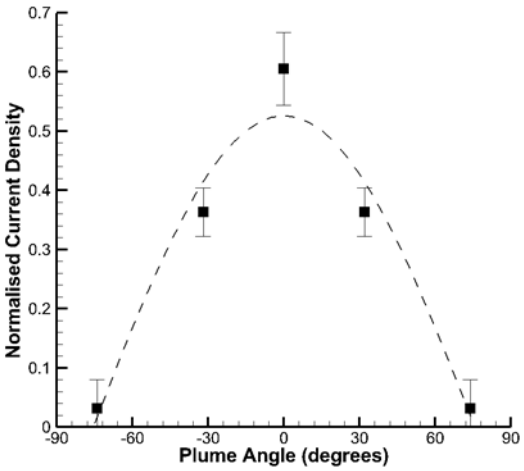

Figure 16: Normalised plume distribution data from the P-BMVAT and its fitted cosine distribution.

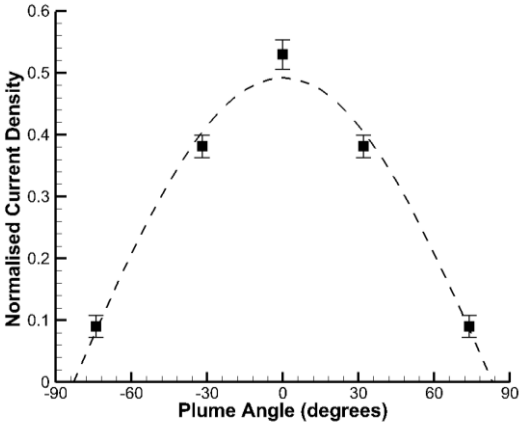

Figure 17: Normalised plume distribution data from the M-BMVAT using the aluminium cathode.

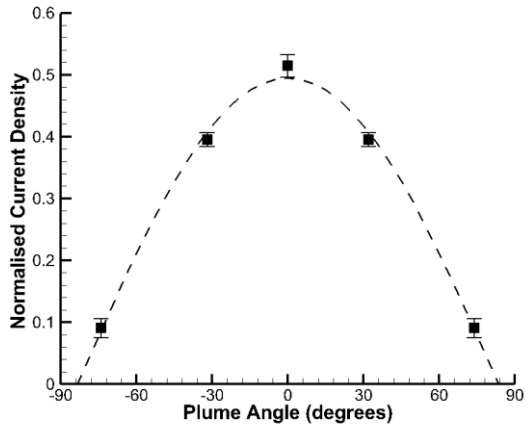

Figure 18: Normalised plume distribution data using the M-BMVAT using the aluminium cathode.

The plume divergence angle, defined as the angle within which 95 % of the ion current is observed, and C_t, the thrust correction factor can be calculated from the fitted cosine distribution equation. Table 5 presents these values and Figure 19 shows an image of a single pulse where the plume divergence can be visually observed.

Table 5: Plume divergence angle and C_t for each of the VATs tested.

VAT	**Plume divergence angle**	**Thrust correction factor, C_t**
P-BMVAT	66.02 °	0.74
M-BMVAT with aluminium cathode	72.82°	0.689
M-BMVAT with copper cathode	72.51°	0.691

The results show strong agreement between the two machined blocks, both in terms of the plume angle and C_t. The P-BMVAT performed marginally better with a more confined plume. This was predicted because of the higher vertical offset between the anode and cathode in the P-BMVAT. It also has a larger spread of results, shown by the larger error bars in Figure 16 compared to Figure 17 and Figure 18. This is presumed to be because of lower manufacturing precision than the M-BMVAT resulting in a larger variation between the centre of the cathode to the centre of the anode for a given pixel.

Figure 19: Image of a single pulse of the M-BMVAT with the aluminium cathode showing the plume divergence angle.

5.2 Endurance Results

Pulses have been delivered from the M-BMVAT to the three VATs until the recorded discharge current is less than 1 μs when averaged over 512 pulses. The number of the pulses delivered before this condition was met is as follows:

- 3 million for the P-BMVAT.
- 0.12 million for the M-BMVAT with the aluminium cathode.
- 0.05 million for the M-BMVAT with the copper cathode.

The P-BMVAT has been taken to an electron microscope where an image of each of the 25 pixels was taken to show the erosion of the cathode. Figure 20 combines each of these 25 images in the pixel configuration of the P-BMVAT block. The amount of cathode erosion varied significantly between the pixels, from nearly no erosion as shown in the bottom left pixel, to most the cathode eroded like that seen in the top left pixel. In all, 10 of the 25 pixels showed little to no signs of erosion.

The annular erosion pattern demonstrates that the cathode spot was not able to propagate to the centre of the pixel. This indicates that higher energy pulses are required to achieve full mass utilisation of the cathode. Further investigation into the curing procedure of the cathode ink and manufacturing of process of the P-BMVAT is required to understand the failure mechanism that led to many of pixels not eroding.

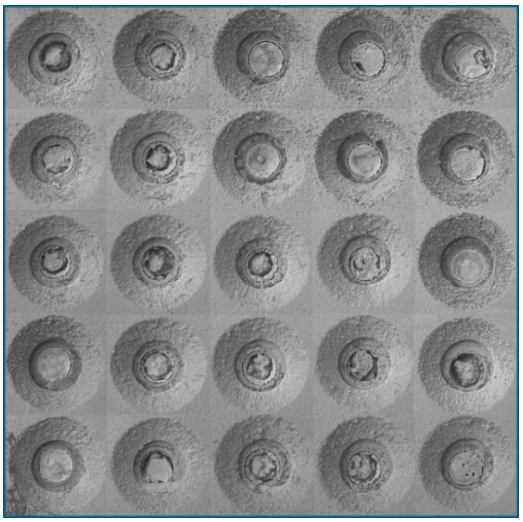

Figure 20: Combined electron microscope images of every pixel of the P-BMVAT after the endurance test.

The duration of the endurance test for the two blocks of the M-BMVAT are far lower than that of the P-BMVAT. Cathode erosion, such that it could be seen with the naked eye, is not present for these two VATs. This demonstrates that the replenishment rate of the conductive layer during a single pulse is less than that ablated during triggerless ignition as the complete erosion of cathode material was not the failure mechanism.

This demonstrates the printed thruster's ability to operate at lower pulse energies than that of a solid metal cathode. The IPC-605X silver ink used for the cathode material of the P-BMVAT comprised of silver micro-particles held within a siloxane polymer matrix. This structure is weaker than the metallic bonds holding together its solid metal counterpart. This difference in structure is shown by comparing Figure 21, showing the erosion of a cathode spot on a copper cathode, to Figure 22, showing the erosion on the P-BMVAT. In Figure 22, the dominant feature on the micrometre scale is an arrangement of ball-like structures which are the silver micro-particles, whereas in Figure 21, it is the cathode erosion from the vacuum arc.

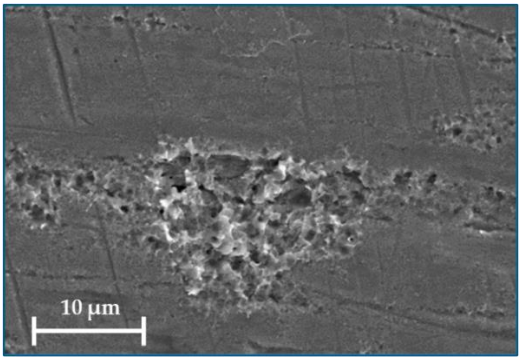

Figure 21: Cathode spot erosion site on the copper cathode after the endurance test.

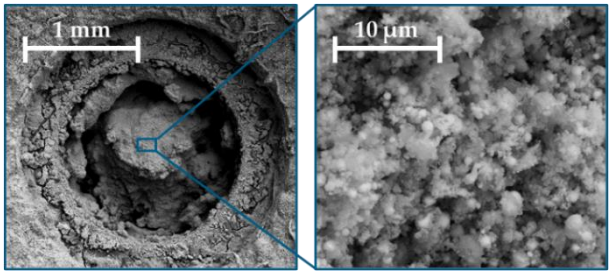

Figure 22: Electron microscope image of an eroded pixel of the P-BMVAT after the endurance test. Whole pixel image on the left and zoomed in image on the right.

6. CONCLUSION

Cube de ALPS has here demonstrated operational capability of an all-printed propulsion system that incorporates printed electronic components and printed thruster architecture. Close agreement was shown in the plume distribution data between the printed vacuum arc thruster and one that was machined. This is in agreement with the literature whereby the distribution is driven by the anode-cathode geometry and opens the door to a wider range of hybrid cathode materials, providing they contain a conductive element. Low energy pulses have been shown to have greater propellant utilisation on a cathode produced from conductive ink. This is a key advantage in nanosatellite applications as it enables a reduction in the size of the power electronics required for sustained operation.

Further characterisation of the plasma plume is required for Cube de ALPS. This shall be done through measuring the total ion current and the ion velocity distribution. These parameters, in connection with the plume distribution data gathered in this study, shall enable a clear performance estimation. The pulse energy shall be increased to enable propagation of the cathode spot to the centre of the pixel. Printed electronic components shall continue to be developed to ensure suitability for the space environment and to obtain their power limitations. The novel printing technology light-out digital manufacturing (LDM), which enables multi-layer and multi-material printing of electronic components shall be investigated for a fully printed electronics configuration.

ACKNOWLEDGMENTS

This work was supported by the European Space Agency through the Innovative Propulsion System for CubeSATs and MicroSATs programme (Grant No. 4000132060/20/NL/RA)**.** We would like to acknowledge Dr Davina Maria Di Cara for technical guidance throughout the technical development element and Luca Bianchi, Martin Eizinger, Maxime Saumier and Siegfried Zoehrer for facilitating the test campaign at ESTEC.

We would also like to acknowledge Robert

Roozeman for guidance and assistance on printed electronics in the first months of the project.

REFERENCES

[1] J. E. Polk, M. J. Sekerak, J. K. Ziemer, J. Schein, N. Qi, and A. Anders, "A theoretical analysis of vacuum arc thruster and vacuum arc ion thruster performance," *IEEE Trans. Plasma Sci.*, vol. 36, no. 5 PART 1, pp. 2167–2179, 2008, doi: 10.1109/TPS.2008.2004374.

[2] A. Anders, "Tracking down the origin of arc plasma science-II. Early continuous discharges," *IEEE Trans. Plasma Sci.*, vol. 31, no. 5 II, pp. 1060–1069, Oct. 2003, doi: 10.1109/TPS.2003.815477.

[3] I. I. Beilis, "State of the theory of vacuum arcs," *IEEE Trans. Plasma Sci.*, vol. 29, no. 5 I, pp. 657–670, Oct. 2001, doi: 10.1109/27.964451.

[4] D. M. S. and P. J. M. Raymond L. Boxman, *Handbook of Vacuum Arc Science and Technology | ScienceDirect*. New Jersey : Noyes Publications, 1996. Accessed: Feb. 24, 2021. [Online]. Available: https://www.sciencedirect.com/book/9780815513759/handbook-of-vacuum-arc-science-and-technology

[5] I. Beilis, "Theoretical Modeling of Cathode Spot Phenomena," *Handb. Vac. Arc Sci. Technol.*, pp. 208–256, 1996, doi: 10.1016/b978-081551375-9.50008-4.

[6] J. Kolbeck, A. Anders, I. I. Beilis, and M. Keidar, "Micro-propulsion based on vacuum arcs," *J. Appl. Phys*, vol. 125, p. 220902, 2019, doi: 10.1063/1.5081096.

[7] A. Anders, I. G. Brown, R. A. MacGill, and M. R. Dickinson, "'Triggerless' triggering of vacuum arcs," *J. Phys. D. Appl. Phys.*, vol. 31, no. 5, pp. 584–587, Mar. 1998, doi: 10.1088/0022-3727/31/5/015.

[8] J. Schein *et al.*, "Inductive energy storage driven vacuum arc thruster," *Rev. Sci. Instrum.*, vol. 73, no. 2 II, p. 925, 2002, doi: 10.1063/1.1428784.

[9] Y. H. Li, J. Y. Pan, and G. Herdrich, "Design and demonstration of micro-scale vacuum cathode arc thruster with inductive energy storage circuit," *Acta Astronaut.*, vol. 172, no. May 2019, pp. 33–46, 2020, doi: 10.1016/j.actaastro.2020.03.012.

[10] S. S. Mohan, M. D. M. Hershenson, S. P. Boyd, and T. H. Lee, "Simple accurate expressions for planar spiral inductances," *IEEE J. Solid-State Circuits*, vol. 34, no. 10, pp. 1419–1420, 1999, doi: 10.1109/4.792620.

[11] "Dielectric Constant: Definition, Units, Formula, Plastic Values &Material List." https://omnexus.specialchem.com/polymer-properties/properties/dielectric-constant (accessed Apr. 12, 2022).